

# Exploring Hot Gas at Junctions of Galaxy Filaments with Suzaku

Ikuyuki Mitsuishi<sup>1</sup>, Hajime Kawahara<sup>2</sup>, Norio Sekiya<sup>3</sup>, Shin Sasaki<sup>1</sup>,

Thierry Sousbie<sup>4</sup> & Noriko Y. Yamasaki<sup>3</sup>

<sup>1</sup>Department of Physics, Tokyo Metropolitan University, Hachioji, Tokyo 192-0397, Japan

<sup>2</sup>Department of Earth and Planetary Science, The University of Tokyo,

7-3-1 Hongo, Bunkyo-ku, Tokyo 113-0033, Japan

<sup>3</sup>Institute of Space and Astronautical Science, Japan Aerospace Exploration Agency,

3-1-1 Yoshinodai, Chuo, Sagamihara, Kanagawa 252-5210, Japan

<sup>4</sup>Institut d'Astrophysique de Paris - 98 bis boulevard Arago, F-75014 Paris, France

`mitsuisi@phys.se.tmu.ac.jp`

Received \_\_\_\_\_; accepted \_\_\_\_\_

## ABSTRACT

We performed five pointing observations with *Suzaku* to search for hot gases associated with the junctions of galaxy filaments where no significant diffuse X-ray sources were detected so far. We discovered X-ray sources successfully in all five regions and analyzed two bright sources in each field. Spectral analysis indicates that three sources originate from X-ray diffuse halos associated with optically bright galaxies or groups of galaxies with  $kT \sim 0.6\text{--}0.8$  keV. Other three sources are possibly group- and cluster-scale X-ray halos with temperatures of  $\sim 1$  keV and  $\sim 4$  keV, respectively while the others are compact object origins such as AGNs. All the three observed intracluster media within the junctions of the galaxy filaments previously found are involved in ongoing mergers. Thus, we demonstrate that deep X-ray observations at the filament junctions identified by galaxy surveys are a powerful mean to explore growing halos in a hierarchical structure undetected so far.

*Subject headings:* galaxies: groups — large scale structure — X-rays: galaxies: clusters

## 1. Introduction

In the structure formation theory of the Universe, the filamentary structure is evolved by the density field, while the rare density peaks within the primordial field latterly collapse into halos. Filaments form the highways along which matter and gases are transported from the lower density regions that will latterly form the voids to those high density peaks, located at their junctions. Since the galaxy filaments are considered to trace the large scale structure of matter and gases behind, one can use them to search for undetected gas components. For instance, X-ray absorption lines across large galaxy filaments were interpreted as the signal from the missing baryons (Buote et al. 2009; Williams et al. 2010). Massive X-ray clusters are also often discovered at the intersection of two or more filaments (Arnaud et al. 2000; Boschin et al. 2004; Cortese et al. 2004; Braglia et al. 2007; Girardi et al. 2008).

Kawahara et al. (2011) (hereafter Paper I) found a new X-ray halo, which can be interpreted as a merging group, by observing with *Suzaku* satellite at a filamentary junction of galaxies. This filamentary junction was visually identified within the Sloan Digital Sky Survey (SDSS) and no X-ray detection was previously achieved. The detection of a new merging group by X-ray can be performed due to *Suzaku*'s high sensitivity coming from low background capability. The evaluation of hot X-ray emitting gas associated with the large scale structure namely an intracluster medium (ICM) in the low- $z$  Universe will enable us to estimate the actual population of baryons. In this paper, we report the further detection of ten new X-ray signals with *Suzaku* by a similar method to Paper I, however, with more sophisticated identification of galaxy filaments by the filament extractor, DisPerSE (Sousbie 2011; Sousbie et al. 2011). Throughout this paper, we assume a  $\Lambda$ CDM universe with  $\Omega_m = 0.27$ ,  $\Omega_\Lambda = 0.73$ , and  $h_0 = 0.7$ . Unless otherwise specified, all errors in text and tables are at 90 % confidence level, and those in figures are at  $1 \sigma$  level.

## 2. Field Selection and Observations

Three-dimensional filamentary structures were extracted based on the spectroscopic data of the SDSS Data Release 7.2 and the filament extractor, DisPerSE which visually allows for the coherent multiscale identification of all types of astrophysical structures, i.e., the voids, walls, filaments and clusters, utilizing the discrete Morse theory (Sousbie 2011; Sousbie et al. 2011). Many filamentary junctions were identified and some of them already have been known as clusters of galaxies and groups of galaxies surrounded by X-ray halos. Among unidentified filamentary junctions, we selected five fields (hereafter FJ1, FJ2, FJ3, FJ4 and FJ5) satisfying the following criterion in the nearby Universe with the redshift between 0.05 and 0.1, where the field of view (hereafter FOV) of *Suzaku* can cover 1–2 Mpc: (1) no specific X-ray halo associated with the large scale structure was identified by the NASA Extragalactic Database (NED), (2) no strong X-ray signal was detected in the *ROSAT* all-sky map and (3) at least one optically bright galaxy exists. Figure 1 shows resultant three-dimensional filamentary structures computed by DisPerSE. Filament Junction 1 (FJ1) has two optically bright galaxies (SDSS J133646.63+435028.9 & SDSS J133646.14+435038.1) with  $z \sim 0.063$  at the center, which seem almost colliding. The filaments run almost in the same plane perpendicular to the line of sight. Filament Junction 2 (FJ2) has optically bright galaxy (SDSS J095701.27+261027.7) at  $z \sim 0.082$  located in the center of Shakhbazian compact group (ShCG) 188 at  $z = 0.080$  (Tovmassian et al. 2005) and two filaments run perpendicular to and along the line of sight, respectively. Filament Junctions 3, 4 and 5 (FJ3, FJ4 and FJ5) locate at several-filament intersections. They possess optically bright spectroscopic identified galaxies with redshifts of 0.064 (SDSS J100540.53+394508.6), 0.072 (SDSS J110238.41+291525.3) and 0.063 (SDSS J113459.83+210546.2) lying in their center positions. We observed five fields with *Suzaku* (Mitsuda et al. 2007) which has low and stable background and therefore is optimum to search for a faint emission from a halo and three co-aligned CCD chips, i.e., X-ray Imaging

Spectrometer (XIS) (Koyama et al. 2007), with  $18' \times 18'$  squared FOV were used in this work. Neutral hydrogen column densities of the Galaxy toward the FOV and observation logs are summarized in Table 1.

Table 1: *Suzaku* observation logs of five targets.

Field name	Obs. ID	Date	Exposure* [ksec]	(R.A., Dec.) [deg]	$N_H^\dagger$ [ $\times 10^{20} \text{ cm}^{-2}$ ]
Filament Junction 1 (FJ1)	806003010	May 25-26, 2011	45	(204.2, 43.8)	1.4
FJ2	806004010	May 18-20, 2011	57	(149.3, 26.2)	2.8
FJ3	806005010	Apr 21-22, 2011	40	(151.4, 39.7)	1.2
FJ4	807038010	June 8-10, 2012	21	(165.7, 29.2)	1.8
FJ5	807039010	June 10-11, 2012	34	(173.7, 21.1)	2.0

\* Exposure time after the COR screening.

† Neutral hydrogen column densities of the Galaxy based on LAB survey (Kalberla et al. 2005).

### 3. Data Reduction

We applied standard data reduction processing (e.g.,  $\text{ANG\_DIST} < 1.5$ ,  $\text{SAA\_HXD} == 0$ ,  $\text{T\_SAA\_HXD} > 436$ ,  $\text{ELV} > 5$  and  $\text{DYE\_ELV} > 20$ ) and additional cut-off-rigidity (COR) selection ( $\text{COR2} > 8 \text{ GV}$  for FJ1, FJ2, FJ3 and FJ5 and  $\text{COR2} > 12 \text{ GV}$  for FJ4) for all *Suzaku* data before analyzing energy spectra to subtract the non X-ray background (NXB) effectively. The higher COR threshold of 12 GV is needed only for FJ4 to suppress higher background fluctuations. The redistribution matrix files were produced by the `xismfgen` ftool and ancillary response files were prepared by using the `xissimarfgen` ftool (Ishisaki et al. 2007). We assumed an input image to `xissimarfgen` to be a uniform flat sky with a radius of  $20'$ . The NXB was estimated from an accumulated night Earth observation with the ftool `xisnxbgen` (Tawa et al. 2008). In all analysis and data reduction, HEASoft version

6.12 and XSPEC version 12.7.0 were utilized.

## 4. Analysis & Results

### 4.1. X-ray Images for the Filamentary Junctions

Figure 2 shows combined images of XIS0, 1 and 3 detectors with galaxy filaments calculated by DisPerSE having almost the same redshift as the central optically bright galaxies. We adopted the energy band of 0.5–2.0 keV where an excess component is expected to be dominant as is the case of Paper I. Anomalous pixels in the XIS0 detector were excluded and complemented by the XIS3 detector. Brighter regions are found at the center of all the images where optically bright galaxies are present. These regions are denoted as FJn-A ( $n = 1, 2, 3, 4, 5$ ), enclosed with red lines in Figure 2. FJ2-A and FJ5-A show non-spherically symmetric distributions and especially FJ5-A possesses multiple peaks in its surface brightness. There are also several source candidates in all the images excluding the FJn-A regions. We selected the brightest region other than FJn-A in each field as FJn-B, enclosed with magenta lines in Figure 2. Due to the poor statistics and/or their locations near the edge of CCD chips, most sources are hardly distinguishable from point sources based on their surface brightness profiles considering the spatial resolution of the *Suzaku* X-ray telescope (HPD $\sim$ 1.8'). However, especially FJ2-A and FJ5-A show asymmetries and extended features. Hence, we proceeded to spectroscopic analysis only for FJn-A and FJn-B because other candidates do not emit enough photons to discuss the origin through spectral analysis.

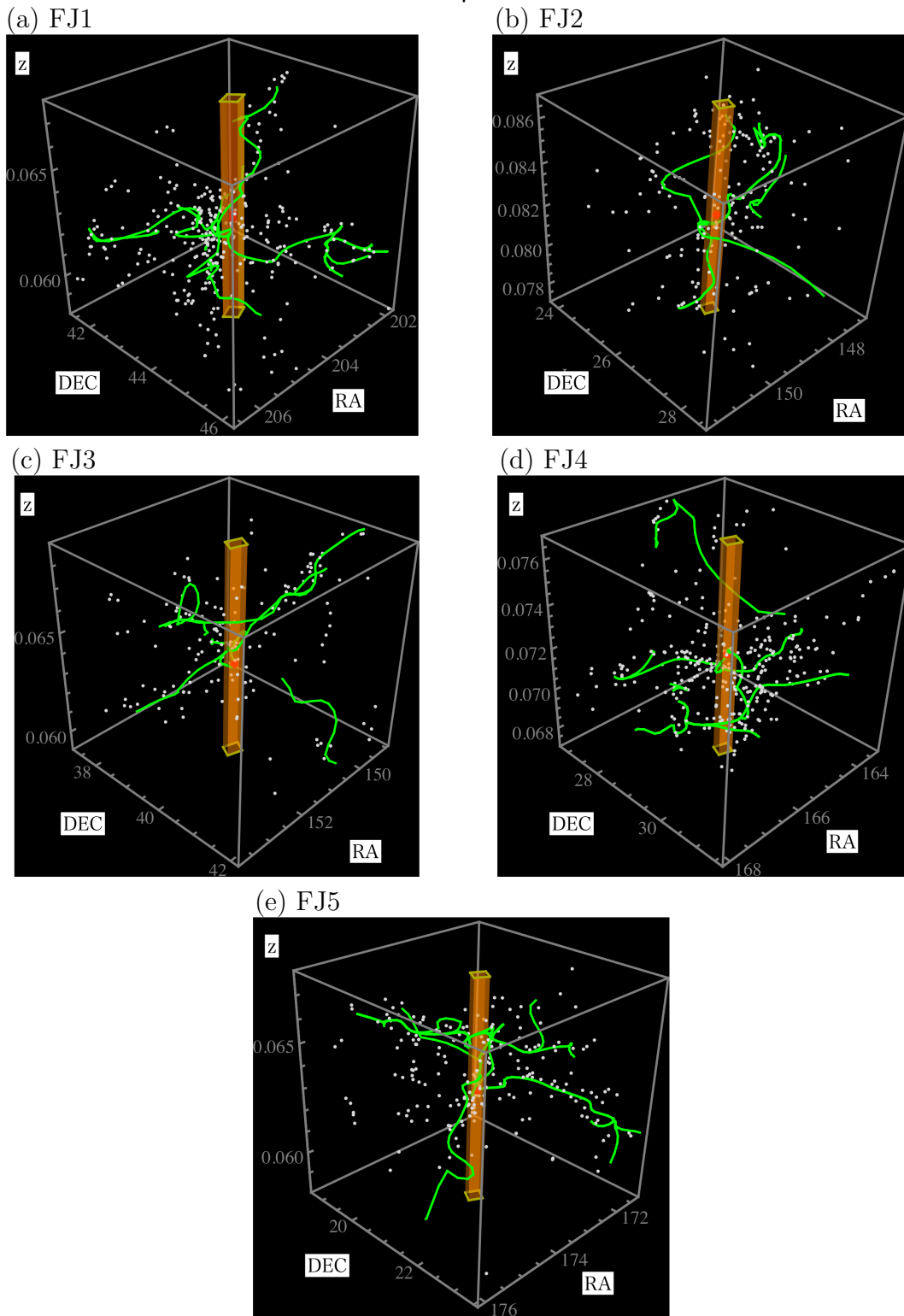


Fig. 1.— The SDSS spectroscopic galaxy distribution around five observed regions, i.e., FJ1 (top left), FJ2 (top right), FJ3 (middle left), FJ4 (middle right) and FJ5 (bottom). White and red dots indicate galaxies and the optically-bright galaxies, respectively. Filamentary structures computed by DisPerSE are represented by green solid curves. The *Suzaku* FOVs are shown by yellow cylinders.

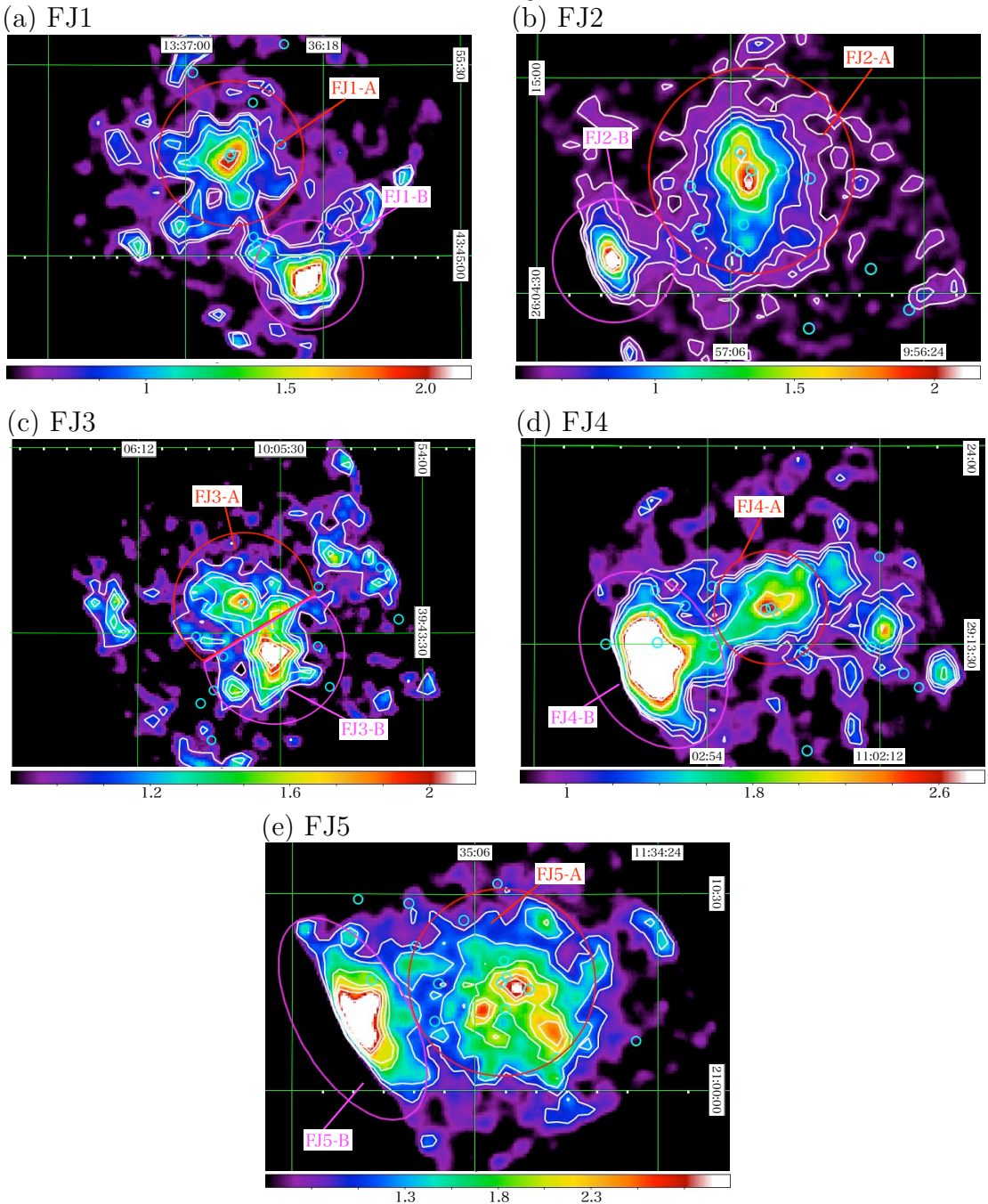


Fig. 2.— The combined images of XIS0, 1 and 3 detectors at the energy range between 0.5 and 2.0 keV in the unit of  $\text{cts} (\text{exposure})^{-1} (64 \text{ pixel})^{-1}$  for all five fields, i.e., FJ1 (top left), FJ2 (top right), FJ3 (middle left), FJ4 (middle right) and FJ5 (bottom). Vignetting correction is not applied. The SDSS spectroscopic identified galaxies (cyan circles) and X-ray contours (white solid lines) are also exhibited. Regions enclosed by red and magenta correspond to the central X-ray emitting regions (FJn-A) where optically-bright galaxies are placed and the brightest regions (FJn-B) other than FJn-A and are used for spectral analysis. To emphasize FJn-A, some pixels in FJn-B are saturated.

## 4.2. Spectral Analysis

We created energy spectra from the filament junction fields as shown in Figure 2 to examine the emission origin. The FJn-A regions including bright sources around optically bright galaxies were extracted by circles with radii of 4 arcmin for FJ1-A, 3 arcmin for FJ4-A and 5 arcmin for FJ2-A and FJ5-A. The center positions of FJn-A correspond to the positions of optically bright galaxies described in §2. The FJn-B regions were extracted by a circle with a radius of 3 arcmin for FJ1-B and FJ2-B and ellipses with major/minor axes of 5/3.5 arcmin for FJ4-B and 6/3 arcmin for FJ5-B, respectively. For FJ3, because the FJ3-B region is partly overlapped with the FJ3-A region the extracted region was not complete circle with a radius of 4 arcmin. In spectral analysis, the energy ranges of 0.8–5.0 keV for the XIS0 and XIS3 detectors and 0.4–5.0 keV for the XIS1 detector were used.

### 4.2.1. Evaluation of X-ray Background

For spectral analysis of a faint X-ray emission, a careful approach on an X-ray background estimation is important. We use a surrounding region in each FOV to evaluate the energy spectrum of the X-ray background. We defined the FJn-BGD region excluding the FJn-A and FJn-B regions in each FOV. We fitted the spectrum in the FJn-BGD regions with the typical X-ray background emission consisting of (1) an unabsorbed thin thermal collisionally-ionized equilibrium (CIE) plasma, (2) an absorbed thin thermal CIE plasma and (3) an absorbed power law (Yoshino et al. 2009). The first two components represent emissions from the Solar-system neighborhood (hereafter solar wind charge exchange: SWCX and Local Hot Bubble: LHB) and Galactic halo (Milky Way Halo: MWH). On the other hand, the last component corresponds to the accumulation of unresolved extragalactic point sources (cosmic X-ray background: CXB) described by an absorbed power-law model with a photon index of 1.4 as shown in Kushino et al. (2002). The following

model was adopted in the XSPEC software:  $apec_{\text{SWCX+LHB}} + phabs_{\text{Galactic}} (apec_{\text{MWH}} + power-law_{\text{CXB}})$ . To consider the systematic error in the different sensors, a constant factor ( $f$ ) was multiplied for the XIS1 and XIS3 detectors (Mitsuishi et al. 2013). Resulting temperatures of the Galactic foreground emission except for the MWH component in FJ2-BGD, FJ3-BGD and FJ5-BGD and surface brightness of the CXB component in all FJn-BGD regions are consistent with typical values reported in previous studies (Yoshino et al. 2009) within the statistical error. The temperatures of MWH in FJ3-BGD and FJ4-BGD are significantly higher than the typical value at a 90 % significance level but consistent within  $4 \sigma$  significance levels. However, the temperature of MWH in FJ5-BGD is significantly higher than the typical value even at a  $4 \sigma$  significance level. Thus, we conducted further spectral analysis for FJ5-BGD in different ways. As the first trial, the higher COR threshold value of 12 GV was imposed to reduce background contributions. However, no difference was found within the statistical error in their best fit values. Although the area of 2 arcmin from the chip edges was removed to diminish systematic uncertainties and the area within 2 arcmin around FJ5-A and FJ5-B was excluded to reduce contaminations from brighter regions considering the *Suzaku* angular resolution (HPD $\sim$ 1.8') any changes were not confirmed within the statistical error. Thus, we concluded that the temperature of MWH in FJ5 is really high. This sort of hot foreground is known to be present especially at low Galactic latitudes (e.g., Yoshino et al. 2009; Masui et al. 2009). Resultant parameters are summarized in Table 2. As stated in the next section, statistical and systematic uncertainties on the X-ray background are taken into account through a simultaneous fitting using FJn-BGD.

Table 2: The results of the model fitting of the five FJn-BGD regions.

Region	$f^*$	$kT_{\text{SWCX+LHB}}$ [keV]	$\text{Norm}_{\text{SWCX+LHB}}^\dagger$	$kT_{\text{MWH}}$ [keV]	$\text{Norm}_{\text{MWH}}^\dagger$	$S_{\text{CXB}}^\ddagger$	$\chi^2/\text{d.o.f}$
FJ1-BGD	$(1.05_{-0.09}^{+0.10}, 1.12_{-0.09}^{+0.10})$	$0.09_{-0.06}^{+0.03}$	$55_{-35}^{+1100}$	$0.23_{-0.03}^{+0.09}$	$4.1_{-2.2}^{+8.3}$	$7.6 \pm 0.5$	131/163
FJ2-BGD	$(1.14_{-0.09}^{+0.08}, 1.11_{-0.08}^{+0.09})$	$0.09 \pm 0.01$	$69_{-30}^{+31}$	$0.67_{-0.09}^{+0.10}$	$1.4 \pm 0.3$	$7.5 \pm 0.5$	187/181
FJ3-BGD	$(1.15_{-0.09}^{+0.10}, 0.93_{-0.08}^{+0.09})$	$0.12 \pm 0.03$	$29_{-14}^{+50}$	$0.81_{-0.12}^{+0.14}$	$1.2 \pm 0.3$	$7.4 \pm 0.5$	136/114
FJ4-BGD	$(1.30_{-0.13}^{+0.15}, 1.06_{-0.11}^{+0.12})$	$0.09_{-0.03}^{+0.04}$	$60_{-43}^{+720}$	$0.28_{-0.09}^{+0.12}$	$3.2_{-1.6}^{+5.8}$	$8.7 \pm 0.7$	106/83
FJ5-BGD	$(1.42_{-0.11}^{+0.12}, 1.04_{-0.09}^{+0.10})$	$0.15_{-0.01}^{+0.02}$	$18_{-4}^{+7}$	$0.97_{-0.11}^{+0.10}$	$2.1 \pm 0.5$	$11 \pm 1$	171/130

\* Constant factors of XIS1 (left) and XIS3 (right) detectors relative to the XIS0 detector.

† Normalization of the *apec* models divided by a solid angle  $\Omega$ , assumed in a uniform-sky ARF calculation (20' radius), i.e.  $\text{Norm} = (1/\Omega) \int n_e n_H dV / (4\pi(1+z)^2 D_A^2) \text{ cm}^{-5} \text{ sr}^{-1}$  in unit of  $10^{-14}$ , where  $D_A$  is the angular diameter distance.

‡ Surface brightness of CXB in the unit of photons  $\text{s}^{-1} \text{ cm}^{-2} \text{ sr}^{-1} \text{ keV}^{-1}$  at 1 keV.

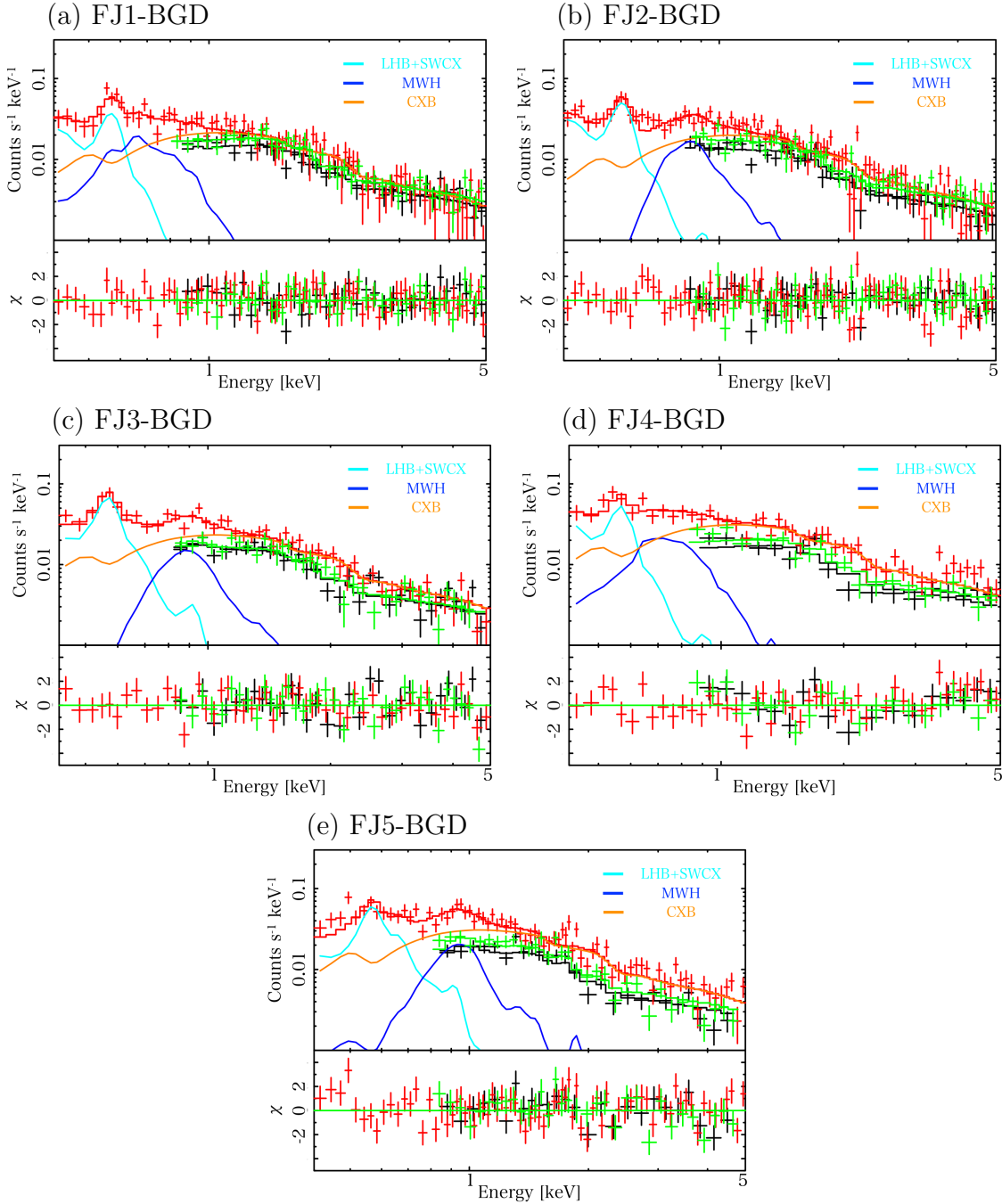


Fig. 3.— XIS0 (black), XIS1 (red) and XIS3 (green) spectra obtained from the FJn-BGD regions, i.e., FJ1-BGD (top left), FJ2-BGD (top right), FJ3-BGD (middle left), FJ4-BGD (middle right) and FJ5-BGD (bottom). Resultant spectra are fitted with the X-ray background emission model, i.e.,  $apec_{SWCX+LHB}$  (cyan) +  $phabs_{Galactic} \times (apec_{MWH}$  (blue) +  $power-law_{CXB}$  (orange)), and the best fit models only for the XIS1 detector are shown for simplicity.

#### 4.2.2. Spectral fitting for FJ sources

We fitted the spectra of both FJn-A and FJn-B with FJn-BGD regions as a template of X-ray background. A simultaneous fitting using the FJn-BGD regions was carried out with common parameters for the background emission ( $kT_{\text{SWCX+LHB}}$ ,  $Norm_{\text{SWCX+LHB}}$ ,  $kT_{\text{MWH}}$ ,  $Norm_{\text{MWH}}$  and  $S_{\text{CXB}}$ ) to consider the statistical and systematic errors. Because the FJn-BGD spectra cannot reproduce all the spectra obtained from FJn-A and FJn-B at all firstly we assumed a thin thermal emission as the excess emissions as with the case of Paper I and then tried a non-thermal emission model.

For FJn-A, we let the abundance of the excess emission vary and then fix it to be 0.3 or 1 solar if the abundance cannot be constrained due to poor statistics. The former value corresponds to the typical abundance in groups of galaxies and clusters of galaxies (e.g., Mulchaey et al. 2003; Baumgartner et al. 2005). The redshift of the excess emission in FJn-A is fixed at that of the central optically bright galaxy. Resultant temperatures of the additional plasmas are  $\sim 0.6$ , 1.3, 0.8, 0.7 and 1.0 keV for FJ1-A, FJ2-A, FJ3-A, FJ4-A and FJ5-A, respectively. The abundance values were constrained only for FJ2-A and FJ5-A and resultant metal abundances are  $0.2 \pm 0.1$  and  $< 0.1$  solar, respectively. Temperatures with the abundance of 0.3 or 1 solar are consistent with each other in all cases. No additional absorption is required for FJn-A. Next, a power-law component was added instead of the thermal component. The goodness of the fit were worse than those in the thermal plasma emission cases for all regions because the power-law component does not make up for the residual around 0.8 keV as shown in Figure 4. Resulting photon indices are  $\sim 3.3$  and 3.6 for FJ2-A and FJ5-A and only lower limits of  $> 4.7$ , 2.5 and 2.7 are obtained for FJ1-A, FJ3-A and FJ4-A, respectively. These values are much higher than the typical value of AGNs (e.g., Winter et al. 2008). Additional absorption on the order of  $10^{21} \text{ cm}^{-2}$  is needed for FJ1-A and FJ2-A. Spectra are shown in Figure 4 and the best fit parameters are summarized in

Table 3.

As is the case with FJn-A, the same spectral analysis was performed also for FJn-B. Although the redshift and the abundance are both regarded as free parameters at first, no reasonable constraint is extracted on the redshift for all the FJn-B sources. Thus, their redshifts of the excess thermal plasmas in FJn-B are set to be 0 and we exhibit only this case. We confirmed that temperatures are consistent with each other in cases of the redshift of free or 0. However, the abundances are well constrained when the redshift of the excess thermal plasma is fixed at 0. The best fit values of temperatures and abundances are  $\sim 1.4, 2.1, 2.6, 1.9$  and  $3.2$  keV with upper limits on the abundance of  $< 0.4, 0.4, 1.4, 0.1$  and  $0.3$  solar for FJ1-B, FJ2-B, FJ3-B, FJ4-B and FJ5-B, respectively. Significant extra absorption is not required for all FJn-B. Then, the thin thermal plasma model was replaced by a power-law component. Photon indices are  $\sim 2.9, 2.3, 2.1, 2.4$  and  $2.0$  for FJ1-B, FJ2-B, FJ3-B, FJ4-B and FJ5-B, respectively. Additional absorption is not requested for the power-law components. Statistically, the thermal and the non-thermal emissions are both acceptable except for FJ4-B while there still remains the residual below 1 keV in the fit with the thin thermal plasma model for FJ4-B. Resultant spectra are shown in Figure 5 and the best fit parameters are summarized in Table 4.

In summary, spectral analysis shows that the thin thermal plasma is preferable in both statistical and physical points of view as the origin for FJn-A since the power-law components cannot make up for the residual around 0.8 keV in the energy spectrum and resulting photon indices are much higher than the typical values of AGNs. For FJn-B, the thin thermal and the non-thermal components are both acceptable statistically. Thus, the origin and corresponding objects utilizing catalogues are discussed in the next section.

## 5. Discussion

### 5.1. Corresponding Object and Origin of FJ sources

In this section, we discuss the origins of the excess sources by searching for corresponding objects in NED.  $L_X$ - $kT$  relation is also utilized to support our discussions. Redshift known galaxies and point sources with/without redshift information are taken into account as supposed candidates of the origin. The spectral analysis as indicated in §4.2.2 demonstrates that FJn-A and FJ4-B prefer thermal and non-thermal origins, respectively, while both thermal and non-thermal components are acceptable for the others. Thus, the preferred component is considered in this discussion.

**FJ1 (A & B):** For FJ1-A, The metal abundance was not constrained and thus 0.3 or 1 solar abundance is assumed for the thin thermal emission. These values correspond to typical values of groups of galaxies (e.g., Mulchaey et al. 2003) and X-ray luminous ( $L_X > 10^{41}$  erg s $^{-1}$ ) early-type galaxies (Matsushita et al. 2000). The derived temperatures of the thin thermal emissions with the abundances of 0.3 and 1 solar are  $\sim 0.6$  keV and consistent with those of typical elliptical galaxies and groups of galaxies (Davis & White 1996; Mulchaey et al. 2003). The observed bolometric X-ray luminosities are  $0.6_{-0.1}^{+0.6} \times 10^{42}$  erg s $^{-1}$ . Thus, the observed  $L_X$ - $kT$  relation also supports the ISM or ICM origin.

For FJ1-B, no difference between the thin thermal plasma model and the power-law component was seen statistically. The resultant temperature is in good agreement with typical values of elliptical galaxies and groups of galaxies. However, no corresponding galaxies are present within a radius of 1.5 arcmin in all redshift planes around the peak in 0.5–2 keV while the nearest radio source (NVSS J133623+434405) is located  $\sim 30$  and 70 arcsec away from the peaks in 0.5–2 keV and 2–5 keV, respectively. Considering the *Suzaku* spatial resolution ( $\sim 1.8'$  in HPD), we cannot reject the possibility of the radio source as the

origin. Thus, we concluded that the origin of FJ1-B is possibly the nearest radio source or X-ray source(s) without any identifications in previous radio and optical surveys in the line of sight.

**FJ2 (A & B):** For FJ2-A, the abundance of the excess thin thermal plasma is well constrained and the resulting abundance is  $0.2 \pm 0.1$  solar, which indicates the ICM origin. The bolometric X-ray luminosity is  $3.5_{-0.6}^{+0.7} \times 10^{42}$  erg s<sup>-1</sup> and the observed  $L_X$ - $kT$  relation is also in accordance with those obtained from groups of galaxies. In conclusion, the observed X-ray halo possibly originates from the hot diffuse halo associated with the group of galaxies, i.e., ShCG 188 where the central optically bright galaxy belongs. Physical properties of this group are discussed in the next section.

As for FJ2-B, the thin thermal plasma and the power-law component are both acceptable statistically. However, we cannot find any spectroscopically-identified galaxies within a radius of 3 arcmin from the peak position in 0.5–2 keV in the line of sight. Meanwhile, the QSO (SDSS J095733.33+260636.5) lies  $\sim 50$  arcsec away from the peak position in 0.5–2 keV and 2–5 keV and the resultant photon index of  $\sim 2.3$  is consistent with that of QSO (George et al. 2000). The observed X-ray emission in FJ2-B likely comes from the QSO or X-ray source(s) without any detections in radio and optical in the line of sight.

**FJ3 (A & B):** Because no constraint is obtained on the abundance, both the ISM and the ICM are candidates as the origin of FJ3-A. The observed luminosity of  $0.6_{-0.2}^{+0.6} \times 10^{42}$  erg s<sup>-1</sup> is in good agreement with the expected value from the  $L_X$ - $kT$  relation of early-type galaxies and groups of galaxies.

In the case of FJ3-B, considering the fact that no corresponding galaxies exist within a radius of 1 arcmin from the peak in 0.5–2 keV in the line of sight and even the nearest radio

sources (FIRST J100539.1+394327 & FIRST J100520.7+394128) are  $>90$  arcsec apart from the peaks in 0.5–2 keV and 2–5 keV X-ray source(s) in the line of sight is possibly the origin.

**FJ4 (A & B):** As the origin is not distinguishable based on the abundance parameter in spectral analysis due to the poor statistics, ISM and ICM are possible origins of FJ4-A. We confirmed that the observed  $L_X$ - $kT$  relation of  $0.3_{-0.1}^{+2.2} \times 10^{42}$  erg s $^{-1}$  and  $\sim 0.7$  keV also reach the same conclusion.

In contrast to FJ4-A, the power-law component with the photon index of  $\sim 2.3$  is favorable rather than the thermal plasma to explain the soft band below 0.8 keV in its energy spectrum. Two QSOs (2MASSi J1103075+291230 & SDSS J110307.58+291230.0) lie very close ( $\sim 10$  arcsec) to the peaks in both 0.5–2 keV and 2–5 keV and are spatially overlapped at almost the same redshift plane of  $\sim 0.37$ . We conducted spectral analysis using the power-law component with the redshift of 0.37 as shown in Table 4 and the derived photon index and luminosity of  $\sim 2.4$  and  $\sim 1 \times 10^{44}$  erg s $^{-1}$  are in good agreement with those of QSO (George et al. 2000). Thus, these observational results lead to a conclusion that background QSO(s) is responsible for the excess emission detected in FJ4-B.

**FJ5 (A & B):** Resultant temperature, abundance and luminosity of  $\sim 1$  keV,  $< 0.1$  and  $3.6_{-0.9}^{+0.5} \times 10^{42}$  erg s $^{-1}$  indicate the ICM origin. Details on FJ5-A are discussed in the next section.

Finally, we discuss the origin of FJ5-B. No statistical significant difference is found in spectral analysis adopting the power-law component or the thin thermal plasma as the excess emission. The photon index of  $\sim 2.0$  is slightly higher than that of the typical value of AGN and the X-ray source (1RXS J113534.0+210228) is present  $\sim 50''$  and  $120''$  away

from the peaks in 0.5–2 keV and 2–5 keV, respectively. Thus, the known X-ray source is not necessarily the origin of FJ5-B because the peak positions in both the soft and the hard bands are distant from the X-ray source even though the large *Suzaku* spatial resolution (1.8' in HPD) is taken into account. Next, we study the possibility of the thin thermal plasma origin. Considering the resulting temperature of  $\sim 3.2$  keV, FJ5-B is considered to be a halo associated with a low temperature cluster of galaxies. Actually, three optically-identified clusters of galaxies, i.e., WHL J113535.6+210333, GMBCG J173.89411+21.04810 and NSC J113528+210301, are located  $\sim 30$ , 60 and 60 arcsec apart from the peak in 0.5–2 keV at the redshifts of  $\sim 0.16$ , 0.17 and 0.11, respectively. Elongations of 60 arcsec correspond to physical distances of  $\sim 100$ -200 kpc at the redshift planes of 0.11, 0.16 and 0.17 which are much smaller than a Mpc-scale typical virial radius of clusters of galaxies. We confirmed that another filamentary junction surely exists in the FJ5-B region at the redshift plane between 0.16 and 0.17. A filamentary junction at the redshift of  $\sim 0.11$  was not found presumably due to a small number of spectroscopic galaxies. Spectral fittings assuming their redshifts to be 0.11, 0.16 and 0.17 are performed. Resultant temperatures, abundance and luminosities are ( $\sim 3.5$  keV,  $\sim 3.7$  keV,  $\sim 3.8$  keV), ( $< 0.7$  solar,  $< 0.8$  solar,  $< 0.9$  solar) and  $(7.9 \pm 1.5, 15 \pm 3, 15 \pm 3) \times 10^{42}$  erg s $^{-1}$ , respectively. The abundances are not well constrained but do not deny the possibility of the hot halo origin associated with the background cluster(s) of galaxies. The observed luminosities are about an order of magnitude smaller than the expected values from the  $L_X$ - $kT$  relation for clusters of galaxies. However, the *Suzaku* FOV does not cover the whole clusters of galaxies. Thus, in conclusion, the origin of FJ5-B is likely the optically-identified background cluster(s) of galaxies.

The observed  $L_X$ - $kT$  relation of FJ sources is shown in Figure 6 with previous works obtained from early-type galaxies, groups of galaxies and clusters of galaxies (White et al. 1997; Xue & Wu 2000; O'Sullivan et al. 2003) for comparison and the possible origins and corresponding objects for FJ sources discussed above is summarized in Table 5. Note that

luminosities for FJ sources without redshift information were not calculated and therefore Figure 6 does not include them.

## 5.2. Physical Condition in Galaxy Filamentary Junction

Here, we discuss environmental specificity, i.e., galaxy filamentary junctions, in terms of structure formation which we can straightforwardly expect its speciality compared to other fields.

Among five fields, two active interactions are confirmed in FJ2-A and FJ5-A. In FJ2-A, the enlarged halos of the two brightest galaxies in optical R band including the central S0 galaxy in the group ShCG 188 are observed and one of the halo is directed towards another as shown in Tovmassian et al. (2005), which suggests that the group is experiencing an ongoing major merger event because a single massive galaxy can be the responsible perturber in groups. It is also suggested that one more member galaxy is involved in the interaction because the bulge of the galaxy is shifted towards the interacting galaxies. This elongated feature is confirmed also in its X-ray image as shown in Figure 2 and its direction is consistent with that observed in optical. Therefore, in combination with X-ray spectroscopic analysis, the observed X-ray hot gas may originate from ICM associated with the merging event as observed in optical although further detailed analysis with higher spatial resolution is needed.

As for FJ5-A, it holds the multiple peaks and irregular morphology in its surface brightness and no corresponding optically bright elliptical galaxies are present in the peaks. These observational features are seen in groups of galaxies and clusters of galaxies experiencing ongoing mergers (e.g., Kawahara et al. 2011; David & Kempner 2004). Thus, we conclude that the observed X-ray emission derives from the ICM associated with the

ongoing merger event. Although as is the case with Paper I, we searched for a hot spot based on a hardness ratio map, no hot spot was found. X-ray observatories with higher spatial resolution have the potential to detect such a local structure.

As discussed above and in §5.1, three of six diffuse sources are possibly group- and cluster-scale X-ray halo origins and four such samples in the total six pointing observations are discovered from the junctions of galaxy filaments (Paper I and this work). Their fluxes in 0.5–2 keV are  $(2\text{--}4)\times 10^{-13}$  erg s<sup>-1</sup> cm<sup>-2</sup>. According to an integral log N–log S relation for X-ray selected groups of galaxies and clusters of galaxies (e.g., Jones et al. 2002),  $\sim 0.04$  targets in the *Suzaku* FOV are expected assuming the detection limit of  $2\times 10^{-13}$  erg s<sup>-1</sup> cm<sup>-2</sup> in 0.5–2 keV. Thus, it is indicated that our method can extract an X-ray diffuse halo associated with a large scale structure efficiently. Similarly, because resultant fluxes for four compact objects are  $(0.2\text{--}6)\times 10^{-13}$  erg s<sup>-1</sup> cm<sup>-2</sup> in 2–10 keV, the expected number of X-ray point sources within the *Suzaku* FOV is  $\sim 0.9$  when the typical detection limit is assumed to be  $10^{-13}$  erg s<sup>-1</sup> cm<sup>-2</sup> in 2–10 keV (Kushino et al. 2002). Our samples includes two ICMs experiencing ongoing mergers and thus we discovered three ongoing merging groups of galaxies in total by adding the result of Paper I in spite of rare events observationally. X-ray hot gas associated with an optically-bright elliptical galaxy will be detected with a deep X-ray observation while an X-ray halo involved in a large scale structure such as ICM is not necessarily observed from surroundings of an elliptical galaxy. In summary, our results indicate that a galaxy filamentary junction is more than likely to possess X-ray emitting hot gas associated with the large scale structure and have high chances to occur for a merger phenomenon.

X-ray selected survey provides us with new insights in a sequence of a merging phenomena such as fossil groups which is considered to be the end result evolutionally. Hence, we hope that our results on the basis of this optically-selected survey play

a complementary role in the structure evolution towards clusters of galaxies from groups in conjunction with future X-ray selected surveys, such as eROSITA on board Spectrum-Roentgen-Gamma observatory (Cappelluti et al. 2011) and *DIOS* (Ohashi et al. 2010).

## 6. Conclusions

Five X-ray pointing observations were conducted with *Suzaku*. We selected five regions (FJ1, FJ2, FJ3, FJ4 and FJ5) located on junctions of filamentary structures in the galaxy distribution based on SDSS identified by the filament extractor, DisPerSE. Significant X-ray signals were successfully detected in both images and energy spectra and we performed spectroscopic analysis for two bright sources in each field. Spectral analysis demonstrated that their emissions from six sources originate from diffuse halos such as ISM and ICM while the others are compact object origins. Among six diffuse emissions, two of them are group-scale diffuse X-ray halo origins and one is serendipitously-detected background cluster(s) of galaxies. ISM and ICM are both acceptable for other three sources due to the poor statistics. The observed two ICMS are associated with ongoing group-scale merging events. Thus, we conclude that galaxy filamentary junctions have tendency to hold X-ray emitting hot gas involved in the large scale structure and merger events are more likely to happen in such active fields.

This work was supported by Grant-in-Aid for JSPS Fellows 12J07045 and 12J10673 and JSPS KAKENHI Grant Number 25800106.

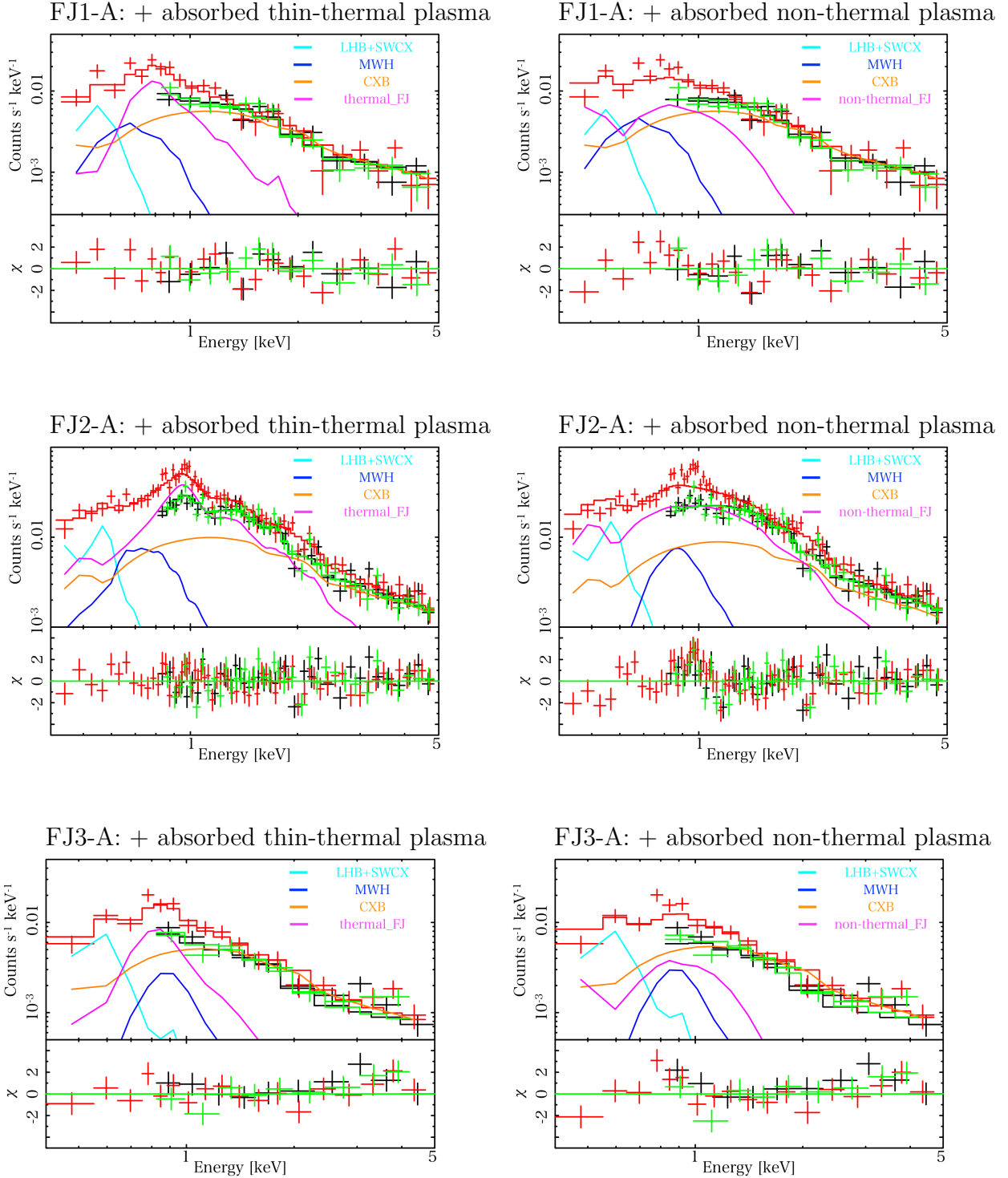


Fig. 4.— The spectra obtained from FJn-A regions, i.e., FJ1-A, FJ2-A, FJ3-A, FJ4-A and FJ5-A, are shown in increasing order from top to bottom. As the excess component, absorbed thin thermal plasma (left) or absorbed power-law (right) component was added for the X-ray background emission.

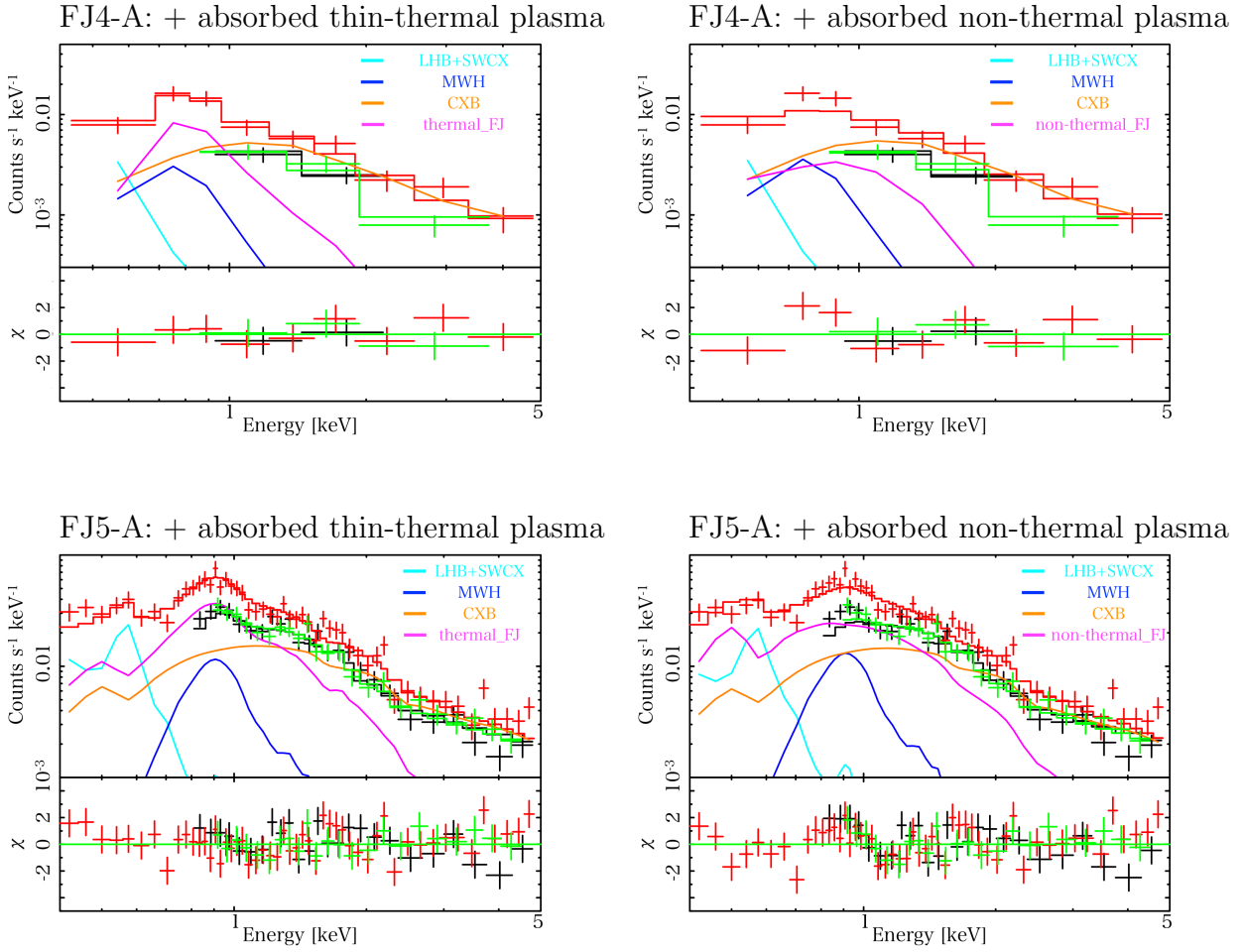


Fig. 4.— continued.

Table 3: The results of model fitting of the five FJn-A regions.

Model: $apec_{\text{SWCX+LHB}} + phabs \times (apec_{\text{MWH}} + pow\text{-law}_{\text{CXB}} + phabs_{\text{FJ}} \times apec_{\text{FJ}})$						
Region	$f_{\text{bgd}}^*$	$kT_{\text{SWCX+LHB}}$ [keV]	$\text{Norm}^\dagger_{\text{SWCX+LHB}}$	$kT_{\text{MWH}}$ [keV]	$\text{Norm}^\dagger_{\text{MWH}}$	$S_{\text{CXB}}^\ddagger$
	$f_{\text{FJ}}^*$	$N_{\text{H:FJ}} [\times 10^{21} \text{ cm}^{-2}]$	$kT_{\text{FJ}}$ [keV]	$Z_{\text{FJ}}^\ddagger [Z_\odot]$	$\text{Norm}^\dagger_{\text{FJ}}$	$\chi^2/\text{d.o.f}$
FJ1-A	$(1.05^{+0.09}_{-0.08}, 1.14 \pm 0.09)$	$0.09^{+0.03}_{-0.06}$	$55^{+72000}_{-34}$	$0.22^{+0.08}_{-0.06}$	$4.2^{+5.4}_{-2.3}$	$7.5 \pm 0.4$
	$(0.95^{+0.10}_{-0.09}, 0.96^{+0.11}_{-0.10})$	<3	$0.61^{+0.11}_{-0.10}$	1 (fix)	$11^{+9}_{-6}$	191/210
↑	$(1.06^{+0.09}_{-0.08}, 1.14 \pm 0.09)$	$0.09^{+0.03}_{-0.06}$	$55^{+50000}_{-33}$	$0.23^{+0.08}_{-0.05}$	$4.1^{+4.6}_{-1.3}$	$7.5 \pm 0.4$
	$(0.94^{+0.10}_{-0.09}, 0.96^{+0.11}_{-0.10})$	<5	$0.62^{+0.12}_{-0.11}$	0.3 (fix)	$22^{+22}_{-5}$	190/210
FJ2-A	$(1.09 \pm 0.08, 1.09 \pm 0.08)$	$0.09^{+0.01}_{-0.02}$	$75^{+170}_{-30}$	$0.28 \pm 0.05$	$3.7^{+2.3}_{-1.1}$	$8.0 \pm 0.4$
	$(1.07 \pm 0.06, 0.98 \pm 0.06)$	<2	$1.3 \pm 0.1$	$0.2 \pm 0.1$	$77^{+15}_{-12}$	343/319
FJ3-A	$(1.11^{+0.09}_{-0.08}, 0.90^{+0.08}_{-0.07})$	$0.12^{+0.03}_{-0.02}$	$28^{+33}_{-13}$	$0.79 \pm 0.13$	$1.1 \pm 0.3$	$7.8^{+0.2}_{-0.5}$
	$(1.13 \pm 0.12, 1.04^{+0.15}_{-0.14})$	<2	$0.76^{+0.15}_{-0.16}$	1 (fix)	$4.7^{+7.2}_{-1.4}$	176/146
↑	$(1.12^{+0.09}_{-0.08}, 0.90^{+0.08}_{-0.07})$	$0.12 \pm 0.02$	$27^{+29}_{-12}$	$0.79^{+0.12}_{-0.13}$	$1.1^{+0.2}_{-0.3}$	$7.8^{+0.3}_{-0.5}$
	$(1.11^{+0.14}_{-0.13}, 1.03^{+0.16}_{-0.15})$	<2	$0.76^{+0.14}_{-0.15}$	0.3 (fix)	$12^{+12}_{-4}$	178/146
FJ4-A	$(1.31^{+0.14}_{-0.13}, 1.06^{+0.12}_{-0.11})$	$0.09^{+0.04}_{-0.05}$	$60^{+800}_{-43}$	$0.28^{+0.12}_{-0.09}$	$3.2^{+5.7}_{-1.6}$	$8.7^{+0.5}_{-0.7}$
	$(1.33^{+0.23}_{-0.21}, 0.92^{+0.19}_{-0.18})$	<2	$0.69^{+0.24}_{-0.39}$	1 (fix)	$6.2^{+48}_{-3}$	111/92
↑	$(1.32^{+0.14}_{-0.13}, 1.06^{+0.12}_{-0.11})$	$0.09 \pm 0.04$	$60^{+790}_{-42}$	$0.28^{+0.12}_{-0.08}$	$3.2^{+5.4}_{-1.5}$	$8.6 \pm 0.7$
	$(1.32^{+0.23}_{-0.21}, 0.91^{+0.19}_{-0.18})$	<3	$0.69^{+0.23}_{-0.45}$	0.3 (fix)	$15^{+110}_{-6}$	112/92
FJ5-A	$(1.25^{+0.09}_{-0.08}, 0.93^{+0.08}_{-0.07})$	$0.11 \pm 0.02$	$39^{+57}_{-16}$	$0.88^{+0.09}_{-0.10}$	$2.2 \pm 0.5$	$12^{+0.7}_{-0.6}$
	$(1.16 \pm 0.08, 0.91 \pm 0.07)$	<1	$0.99^{+0.08}_{-0.09}$	<0.1	$86^{+21}_{-12}$	278/224

Model: $apec_{\text{SWCX+LHB}} + phabs \times (apec_{\text{MWH}} + pow\text{-law}_{\text{CXB}} + phabs_{\text{FJ}} \times pow_{\text{FJ}})$						
Region	$f_{\text{bgd}}^*$	$kT_{\text{SWCX+LHB}}$ [keV]	$\text{Norm}^\dagger_{\text{SWCX+LHB}}$	$kT_{\text{MWH}}$ [keV]	$\text{Norm}^\dagger_{\text{MWH}}$	$S_{\text{CXB}}^\ddagger$
	$f_{\text{FJ}}^*$	$N_{\text{H:FJ}} [\times 10^{21} \text{ cm}^{-2}]$	$\Gamma_{\text{FJ}}$	$z_{\text{FJ}}$	$\chi^2/\text{d.o.f}$	
FJ1-A	$(1.05 \pm 0.09, 1.13 \pm 0.09)$	$0.09^{+0.03}_{-0.06}$	$50^{+31000}_{-33}$	$0.23^{+0.07}_{-0.05}$	$4.6^{+6.3}_{-2.5}$	$7.4 \pm 0.4$
	$(0.94^{+0.11}_{-0.10}, 0.95^{+0.11}_{-0.10})$	$6 \pm 4$	>4.7	0 (fix)	208/210	
FJ2-A	$(1.14^{+0.09}_{-0.08}, 1.09^{+0.09}_{-0.08})$	$0.10^{+0.03}_{-0.01}$	$54^{+28}_{-33}$	$0.76^{+0.07}_{-0.07}$	$1.6 \pm 0.3$	$7.4 \pm 0.5$
	$(1.03^{+0.07}_{-0.06}, 0.97^{+0.07}_{-0.06})$	$2 \pm 1$	$3.3^{+0.4}_{-0.3}$	0 (fix)	411/320	
FJ3-A	$(1.10^{+0.09}_{-0.08}, 0.89^{+0.08}_{-0.07})$	$0.14^{+0.01}_{-0.03}$	$18^{+13}_{-4}$	$0.79 \pm 0.13$	$1.2^{+0.4}_{-0.3}$	$7.8 \pm 0.5$
	$(1.18^{+0.15}_{-0.14}, 1.07 \pm 0.15)$	<11	>2.5	0 (fix)	199/146	
FJ4-A	$(1.30^{+0.14}_{-0.13}, 1.06^{+0.12}_{-0.11})$	$0.09 \pm 0.03$	$61^{+550}_{-43}$	$0.29^{+0.11}_{-0.07}$	$3.3^{+2.9}_{-1.5}$	$8.6 \pm 0.7$
	$(1.39^{+0.25}_{-0.23}, 0.93^{+0.21}_{-0.19})$	<12	>2.7	0 (fix)	121/92	
FJ5-A	$(1.40^{+0.11}_{-0.10}, 1.03^{+0.09}_{-0.08})$	$0.11^{+0.04}_{-0.02}$	$35^{+47}_{-17}$	$0.87^{+0.07}_{-0.06}$	$2.5^{+0.5}_{-0.4}$	$11 \pm 1$
	$(1.14^{+0.09}_{-0.08}, 0.90^{+0.08}_{-0.07})$	<3	$3.6^{+0.7}_{-0.5}$	0 (fix)	305/225	

\* Constant factors of XIS1 (left) and XIS3 (right) detectors relative to the XIS0 detector.

† Normalization of the *apec* models divided by a solid angle  $\Omega$ , assumed in a uniform-sky ARF calculation (20' radius), i.e.  $\text{Norm} = (1/\Omega) \int n_e n_H dV / (4\pi(1+z)^2 D_A^2) \text{ cm}^{-5} \text{ sr}^{-1}$  in unit of  $10^{-14}$ , where  $D_A$  is the angular diameter distance.

‡ Surface brightness of the *power-law* model in the unit of  $10^{-8} \text{ erg cm}^{-2} \text{ s}^{-1} \text{ sr}^{-1}$  in 2–10 keV.

‡ Abundance table tabulated in Anders & Grevesse (1989) was adopted.

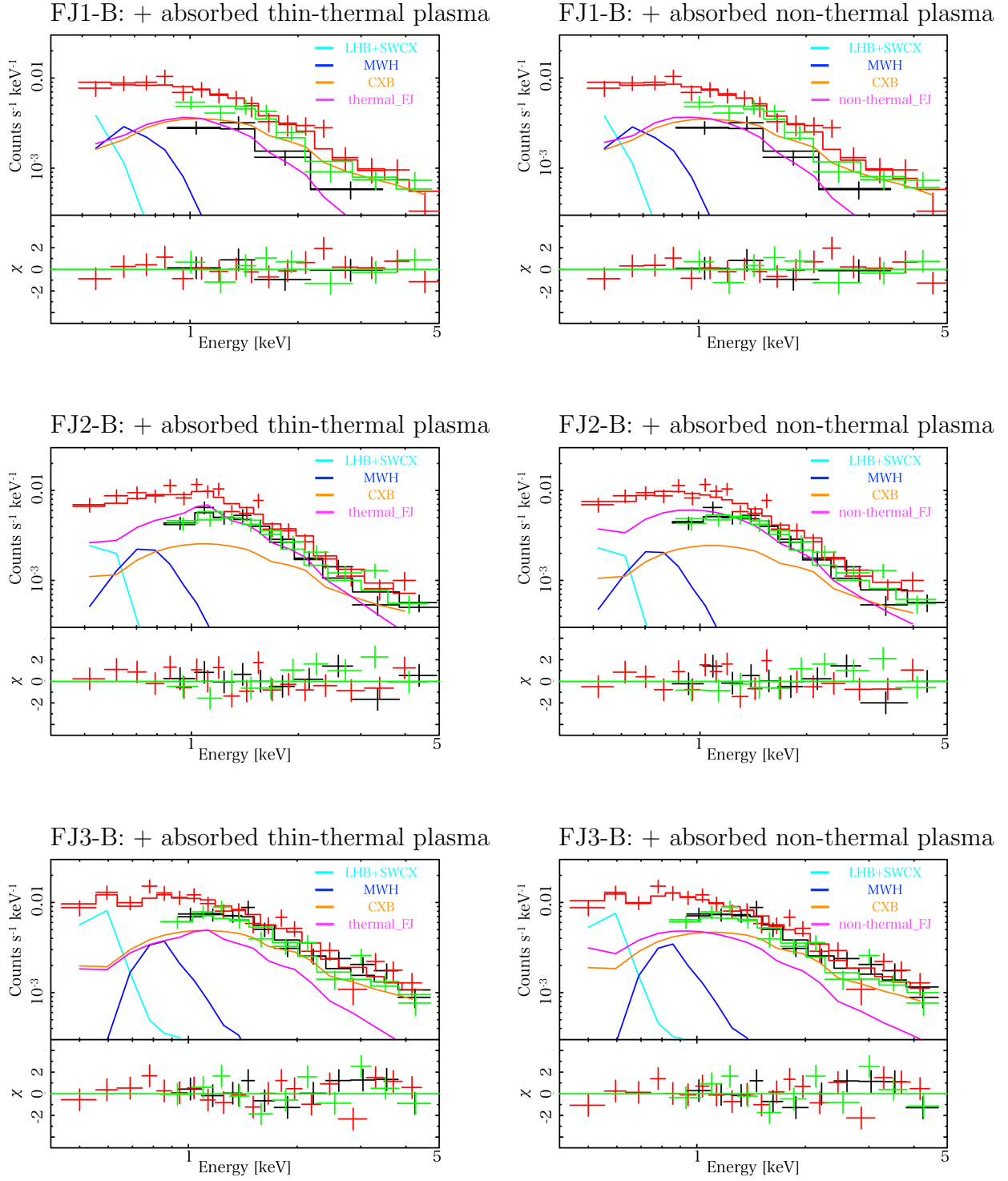


Fig. 5.— The same as Figure 4 but spectra obtained from FJn-B regions.

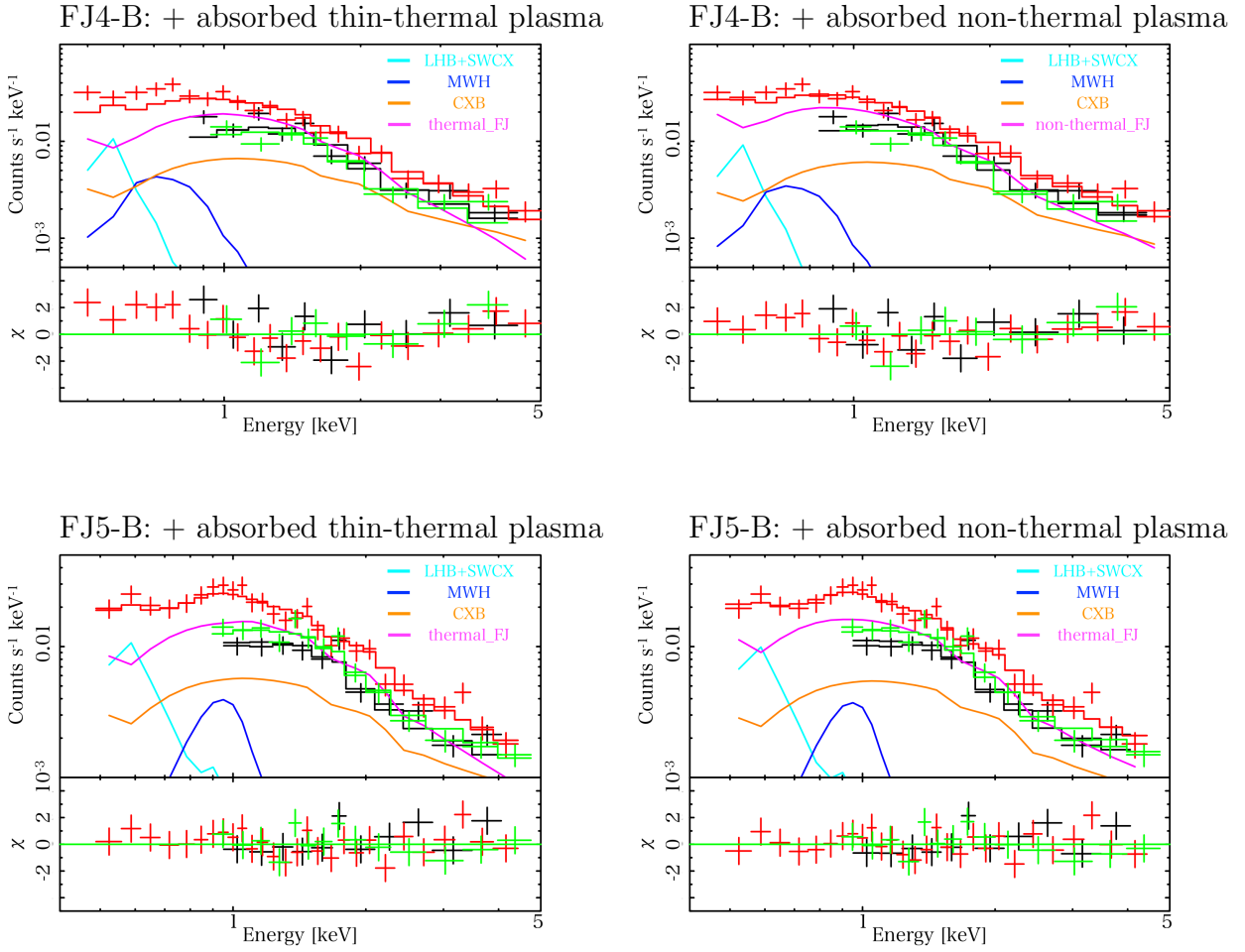


Fig. 5.— continued.

Table 4: The results of model fitting of the five FJn-B regions.

Model: $apec_{\text{SWCX+LHB}} + phabs \times (apec_{\text{MWH}} + pow\text{-}law_{\text{CXB}} + phabs_{\text{FJ}} \times apec_{\text{FJ}})$							
Region	$f_{\text{bgd}}^*$	$kT_{\text{SWCX+LHB}}$ [keV]	$\text{Norm}^{\dagger}_{\text{SWCX+LHB}}$	$kT_{\text{MWH}}$ [keV]	$\text{Norm}^{\dagger}_{\text{MWH}}$	$S^{\ddagger}_{\text{CXB}}$	
	$f_{\text{FJ}}^*$	$N_{\text{H:FJ}}$ [ $\times 10^{21}$ cm $^{-2}$ ]	$kT_{\text{FJ}}$ [keV]	$z_{\text{FJ}}$	$Z^{\ddagger}_{\text{FJ}}$ [ $Z_{\odot}$ ]	$\text{Norm}^{\dagger}_{\text{FJ}}$	$\chi^2/\text{d.o.f}$
FJ1-B	(1.05 $\pm$ 0.09, 1.12 $^{+0.10}_{-0.09}$ )	0.09 $^{+0.03}_{-0.06}$	57 $^{+520}_{-36}$	0.23 $^{+0.08}_{-0.05}$	4.3 $^{+6.4}_{-2.2}$	7.6 $\pm$ 0.5	
	(1.31 $^{+0.25}_{-0.19}$ , 1.23 $^{+0.25}_{-0.16}$ )	<8	1.4 $^{+1.2}_{-0.9}$	0 (fix)	<0.4	38 $^{+150}_{-13}$	149/186
FJ2-B	(1.11 $^{+0.09}_{-0.08}$ , 1.10 $^{+0.04}_{-0.08}$ )	0.07 $\pm$ 0.02	220 $^{+810}_{-140}$	0.30 $^{+0.09}_{-0.05}$	3.5 $^{+1.7}_{-1.1}$	7.8 $\pm$ 0.5	
	(1.20 $^{+0.14}_{-0.12}$ , 1.00 $^{+0.14}_{-0.12}$ )	<1	2.1 $^{+0.7}_{-0.4}$	0 (fix)	<0.4	71 $^{+20}_{-18}$	198/182
FJ3-B	(1.13 $^{+0.10}_{-0.09}$ , 0.92 $^{+0.09}_{-0.08}$ )	0.12 $^{+0.03}_{-0.02}$	29 $^{+42}_{-14}$	0.79 $^{+0.13}_{-0.11}$	1.2 $\pm$ 0.3	7.5 $\pm$ 0.5	
	(0.88 $^{+0.11}_{-0.10}$ , 0.90 $^{+0.12}_{-0.11}$ )	<1	2.6 $^{+2.3}_{-1.0}$	0 (fix)	<1.4	31 $^{+14}_{-13}$	183/150
FJ4-B	(1.18 $^{+0.13}_{-0.12}$ , 1.00 $^{+0.11}_{-0.10}$ )	0.09 $^{+0.02}_{-0.04}$	95 $^{+1500}_{-59}$	0.27 $\pm$ 0.08	4.3 $^{+5.6}_{-1.7}$	9.1 $\pm$ 0.7	
	(1.33 $^{+0.16}_{-0.14}$ , 0.88 $^{+0.13}_{-0.11}$ )	<1	1.9 $^{+0.7}_{-0.5}$	0 (fix)	<0.1	110 $^{+28}_{-20}$	186/117
FJ5-B	(1.39 $^{+0.11}_{-0.10}$ , 1.03 $^{+0.09}_{-0.08}$ )	0.15 $^{+0.02}_{-0.01}$	18 $\pm$ 4	0.97 $^{+0.09}_{-0.11}$	2.2 $\pm$ 0.5	11 $\pm$ 1	
	(1.39 $^{+0.14}_{-0.12}$ , 1.16 $^{+0.13}_{-0.11}$ )	<1	3.2 $^{+1.0}_{-0.7}$	0 (fix)	<0.3	120 $^{+21}_{-23}$	213/177
↑	(1.39 $^{+0.11}_{-0.10}$ , 1.03 $^{+0.09}_{-0.08}$ )	0.15 $^{+0.02}_{-0.01}$	18 $\pm$ 4	0.97 $^{+0.09}_{-0.11}$	2.2 $\pm$ 0.5	11 $\pm$ 1	
	(1.39 $^{+0.14}_{-0.12}$ , 1.16 $^{+0.13}_{-0.12}$ )	<1	3.5 $^{+1.1}_{-0.7}$	0.11 (fix)	<0.7	140 $\pm$ 28	211/177
↑	(1.25 $^{+0.11}_{-0.10}$ , 0.94 $^{+0.09}_{-0.08}$ )	0.15 $^{+0.02}_{-0.01}$	18 $\pm$ 4	0.97 $^{+0.09}_{-0.11}$	2.2 $\pm$ 0.5	11 $\pm$ 1	
	(1.39 $^{+0.14}_{-0.12}$ , 1.15 $^{+0.13}_{-0.12}$ )	<1	3.7 $^{+1.1}_{-0.7}$	0.16 (fix)	<0.8	150 $\pm$ 30	211/177
↑	(1.39 $^{+0.11}_{-0.10}$ , 1.03 $^{+0.09}_{-0.08}$ )	0.15 $^{+0.02}_{-0.01}$	18 $\pm$ 4	0.97 $^{+0.09}_{-0.11}$	2.2 $\pm$ 0.5	11 $\pm$	
	(1.39 $^{+0.14}_{-0.12}$ , 1.14 $^{+0.13}_{-0.11}$ )	<1	3.8 $^{+1.0}_{-0.8}$	0.17 (fix)	<0.9	150 $^{+30}_{-32}$	211/177

Model: $apec_{\text{SWCX+LHB}} + phabs \times (apec_{\text{MWH}} + pow\text{-}law_{\text{CXB}} + phabs_{\text{FJ}} \times pow_{\text{FJ}})$							
Region	$f_{\text{bgd}}^*$	$kT_{\text{SWCX+LHB}}$ [keV]	$\text{Norm}^{\dagger}_{\text{SWCX+LHB}}$	$kT_{\text{MWH}}$ [keV]	$\text{Norm}^{\dagger}_{\text{MWH}}$	$S^{\ddagger}_{\text{CXB}}$	
	$f_{\text{FJ}}^*$	$N_{\text{H:FJ}}$ [ $\times 10^{21}$ cm $^{-2}$ ]	$\Gamma_{\text{FJ}}$	$z_{\text{FJ}}$	$\chi^2/\text{d.o.f}$		
FJ1-B	(1.06 $^{+0.10}_{-0.09}$ , 1.13 $^{+0.10}_{-0.09}$ )	0.09 $^{+0.03}_{-0.06}$	57 $^{+550}_{-36}$	0.23 $^{+0.08}_{-0.05}$	4.3 $^{+7.2}_{-2.2}$	7.6 $\pm$ 0.5	
	(1.30 $^{+0.24}_{-0.20}$ , 1.21 $^{+0.23}_{-0.19}$ )	<6	2.9 $^{+1.7}_{-0.8}$	0 (fix)	149/187		
FJ2-B	(1.15 $^{+0.09}_{-0.08}$ , 1.11 $^{+0.09}_{-0.08}$ )	0.09 $^{+0.01}_{-0.02}$	94 $^{+210}_{-39}$	0.65 $^{+0.09}_{-0.08}$	1.5 $\pm$ 0.3	7.5 $\pm$ 0.5	
	(1.17 $^{+0.15}_{-0.13}$ , 1.00 $^{+0.14}_{-0.12}$ )	<1	2.3 $^{+0.4}_{-0.2}$	0 (fix)	195/183		
FJ3-B	(1.15 $^{+0.10}_{-0.09}$ , 0.93 $^{+0.09}_{-0.08}$ )	0.12 $^{+0.03}_{-0.02}$	29 $^{+44}_{-14}$	0.79 $^{+0.14}_{-0.11}$	1.2 $\pm$ 0.3	7.5 $\pm$ 0.5	
	(0.84 $^{+0.11}_{-0.10}$ , 0.88 $^{+0.12}_{-0.11}$ )	<1	2.1 $\pm$ 0.3	0 (fix)	181/151		
FJ4-B	(1.25 $^{+0.14}_{-0.12}$ , 1.02 $^{+0.12}_{-0.10}$ )	0.09 $^{+0.03}_{-0.05}$	75 $^{+840}_{-50}$	0.27 $^{+0.09}_{-0.07}$	3.6 $^{+7.0}_{-1.6}$	8.9 $\pm$ 0.7	
	(1.23 $^{+0.14}_{-0.12}$ , 0.85 $^{+0.12}_{-0.11}$ )	<1	2.4 $\pm$ 0.2	0 (fix)	156/118		
↑	(1.47 $^{+0.17}_{-0.14}$ , 1.10 $^{+0.12}_{-0.11}$ )	0.09 $^{+0.03}_{-0.05}$	75 $^{+590}_{-49}$	0.27 $^{+0.06}_{-0.09}$	3.6 $^{+4.8}_{-1.4}$	8.9 $\pm$ 0.7	
	(1.21 $^{+0.14}_{-0.12}$ , 0.88 $^{+0.12}_{-0.11}$ )	<1	2.4 $\pm$ 0.2	0.37 (fix)	156/118		
FJ5-B	(1.41 $^{+0.12}_{-0.11}$ , 1.04 $\pm$ 0.09)	0.15 $^{+0.02}_{-0.01}$	18 $^{+7}_{-4}$	0.98 $^{+0.09}_{-0.11}$	2.2 $\pm$ 0.5	11 $\pm$ 1	
	(1.34 $^{+0.14}_{-0.11}$ , 1.13 $^{+0.13}_{-0.11}$ )	<1	2.0 $^{+0.3}_{-0.1}$	0 (fix)	211/178		

\* Constant factors of XIS1 (left) and XIS3 (right) detectors relative to the XIS0 detector.

† Normalization of the *apec* models divided by a solid angle  $\Omega$ , assumed in a uniform-sky ARF calculation (20' radius), i.e.  $\text{Norm} = (1/\Omega) \int n_e n_H dV / (4\pi(1+z)^2 D_A^2) \text{ cm}^{-5} \text{ sr}^{-1}$  in unit of  $10^{-14}$ , where  $D_A$  is the angular diameter distance.

‡ Surface brightness of the *power-law* model in the unit of  $10^{-8} \text{ erg cm}^{-2} \text{ s}^{-1} \text{ sr}^{-1}$  in 2–10 keV.

‡ Abundance table tabulated in Anders & Grevesse (1989) was adopted.

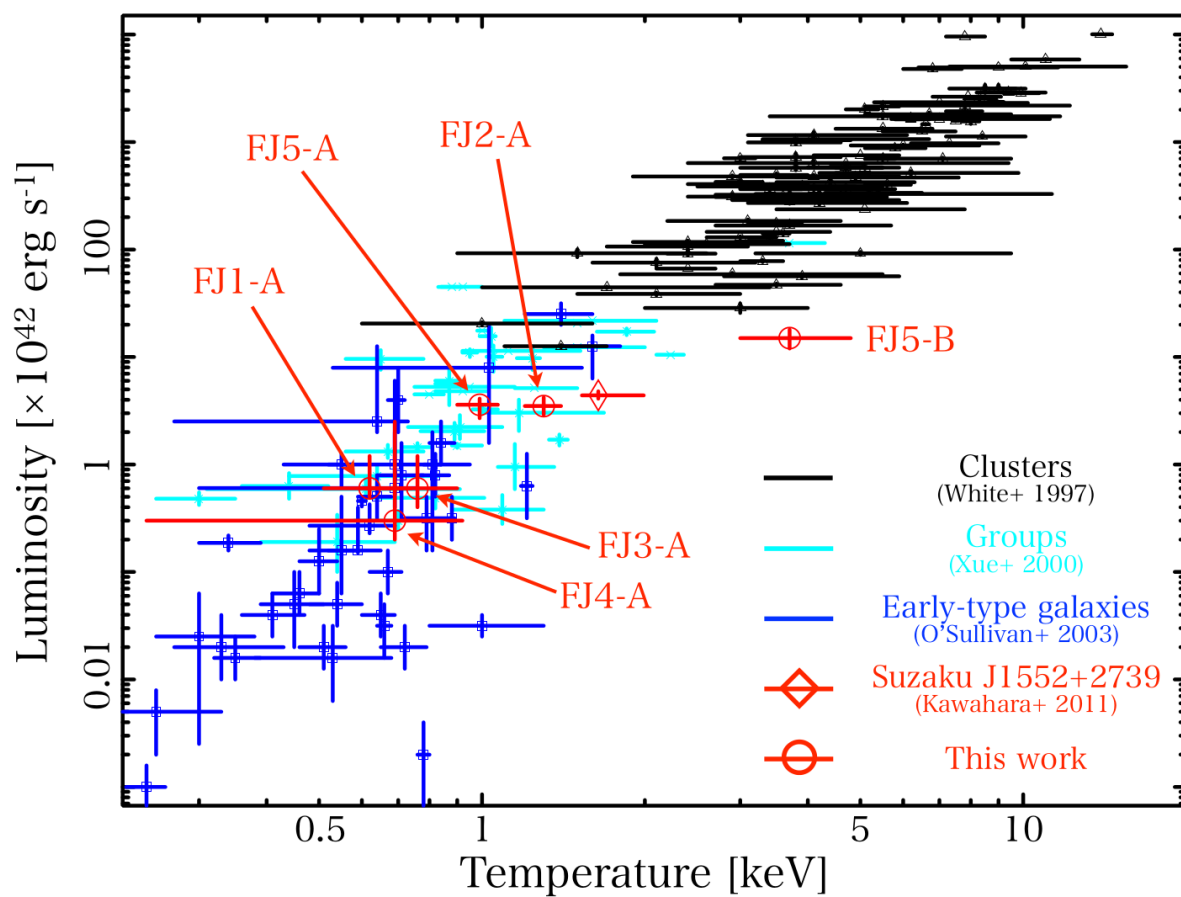


Fig. 6.— The observed  $L_X$ – $kT$  relation of FJ sources including the result of Paper I with previous studies for clusters of galaxies (White et al. 1997), groups of galaxies (Xue & Wu 2000) and early-type galaxies (O’Sullivan et al. 2003).

Table 5: Summary of possible origins and corresponding objects for FJ sources with physical properties.

FJn-A				
Region	$kT^*$ [keV]	$L_X$ [ $\times 10^{42}$ erg s $^{-1}$ ]	Possible origin	
FJ1	$(0.62_{-0.11}^{+0.12}, 0.61_{-0.10}^{+0.11})$	$0.6_{-0.1}^{+0.6}$	ISM or ICM	
FJ2	$1.3 \pm 0.1$	$3.5_{-0.6}^{+0.7}$	ICM	
FJ3	$(0.76_{-0.15}^{+0.14}, 0.76_{-0.16}^{+0.15})$	$0.6_{-0.2}^{+0.6}$	ISM or ICM	
FJ4	$(0.69_{-0.45}^{+0.23}, 0.69_{-0.39}^{+0.24})$	$0.3_{-0.1}^{+2.2}$	ISM or ICM	
FJ5	$0.99_{-0.09}^{+0.08}$	$3.6_{-0.9}^{+0.5}$	ICM	

FJn-B					
Region	$kT$ [keV]	$L_X$ [ $\times 10^{42}$ erg s $^{-1}$ ]	$\Gamma$	$N_H$ [ $\times 10^{21}$ cm $^{-2}$ ]	Possible origin
FJ1			$2.9_{-0.8}^{+1.7}$	$< 6$	radio source (NVSS J133623+434405) or X-ray source(s) in the line of sight
FJ2			$2.3_{-0.2}^{+0.4}$	$< 1$	QSO (SDSS J095733.33+260636.5) or X-ray source(s) in the line of sight
FJ3-B			$2.1 \pm 0.3$	$< 1$	X-ray source(s) in the line of sight
FJ4		120 ( $z = 0.37$ )	$2.4 \pm 0.2$	$< 1$	QSOs (2MASSi J1103075+291230 and/or SDSS J110307.58+291230.0)
FJ5	$3.5_{-0.7}^{+1.1}$	$7.9 \pm 1.5$ ( $z = 0.11$ )			clusters of galaxies (NSC J113528+210301)
	$3.7_{-0.7}^{+1.1}$	$15 \pm 3$ ( $z = 0.16$ )			and/or WHL J113535.6+210333
	$3.8_{-0.8}^{+1.0}$	$15 \pm 3$ ( $z = 0.17$ )			and/or GMBCG J173.89411+21.04810)

\* Values in parentheses correspond to temperatures obtained by assuming the abundances to be 0.3 (left) and 1 (right) solar, respectively.

## REFERENCES

- Anders, E., & Grevesse, N. 1989, *gca*, 53, 197
- Arnaud, M., Maurogordato, S., Slezak, E., & Rho, J. 2000, *A&A*, 355, 461
- Baumgartner, W. H., Loewenstein, M., Horner, D. J., & Mushotzky, R. F. 2005, *ApJ*, 620, 680
- Boschin, W., Girardi, M., Barrena, R., Biviano, A., Feretti, L., & Ramella, M. 2004, *A&A*, 416, 839
- Braglia, F., Pierini, D., & Böhringer, H. 2007, *A&A*, 470, 425
- Buote, D. A., Zappacosta, L., Fang, T., Humphrey, P. J., Gastaldello, F., & Tagliaferri, G. 2009, *ApJ*, 695, 1351
- Cappelluti, N., et al. 2011, *Memorie della Societa Astronomica Italiana Supplementi*, 17, 159
- Cortese, L., Gavazzi, G., Boselli, A., Iglesias-Paramo, J., & Carrasco, L. 2004, *A&A*, 425, 429
- David, L. P., & Kempner, J. 2004, *ApJ*, 613, 831
- Davis, D. S., & White, III, R. E. 1996, *ApJ*, 470, L35
- George, I. M., Turner, T. J., Yaqoob, T., Netzer, H., Laor, A., Mushotzky, R. F., Nandra, K., & Takahashi, T. 2000, *ApJ*, 531, 52
- Girardi, M., Barrena, R., Boschin, W., & Ellingson, E. 2008, *A&A*, 491, 379
- Ishisaki, Y., et al. 2007, *PASJ*, 59, 113
- Jones, L. R., McHardy, I., Newsam, A., & Mason, K. 2002, *MNRAS*, 334, 219

- Kalberla, P. M. W., Burton, W. B., Hartmann, D., Arnal, E. M., Bajaja, E., Morras, R., & Pöppel, W. G. L. 2005, *A&A*, 440, 775
- Kawahara, H., Yoshitake, H., Nishimichi, T., & Sousbie, T. 2011, *ApJ*, 727, L38
- Koyama, K., et al. 2007, *PASJ*, 59, 23
- Kushino, A., Ishisaki, Y., Morita, U., Yamasaki, N. Y., Ishida, M., Ohashi, T., & Ueda, Y. 2002, *PASJ*, 54, 327
- Masui, K., Mitsuda, K., Yamasaki, N. Y., Takei, Y., Kimura, S., Yoshino, T., & McCammon, D. 2009, *PASJ*, 61, 115
- Matsushita, K., Ohashi, T., & Makishima, K. 2000, *PASJ*, 52, 685
- Mitsuda, K., et al. 2007, *PASJ*, 59, 1
- Mitsuishi, I., Yamasaki, N. Y., & Takei, Y. 2013, *PASJ*, 65, 44
- Mulchaey, J. S., Davis, D. S., Mushotzky, R. F., & Burstein, D. 2003, *ApJS*, 145, 39
- Ohashi, T., et al. 2010, in *Society of Photo-Optical Instrumentation Engineers (SPIE) Conference Series*, Vol. 7732, *Society of Photo-Optical Instrumentation Engineers (SPIE) Conference Series*
- O’Sullivan, E., Ponman, T. J., & Collins, R. S. 2003, *MNRAS*, 340, 1375
- Sousbie, T. 2011, *MNRAS*, 414, 350
- Sousbie, T., Pichon, C., & Kawahara, H. 2011, *MNRAS*, 414, 384
- Tawa, N., et al. 2008, *PASJ*, 60, 11
- Tovmassian, H. M., Tiersch, H., Tovmassian, G. H., Chavushyan, V. H., Navarro, S. G., Neizvestny, S., & Torres-Papaqui, J. P. 2005, *Rev. Mexicana Astron. Astrofis.*, 41, 3

White, D. A., Jones, C., & Forman, W. 1997, MNRAS, 292, 419

Williams, R. J., Mulchaey, J. S., Kollmeier, J. A., & Cox, T. J. 2010, ApJ, 724, L25

Winter, L. M., Mushotzky, R. F., Tueller, J., & Markwardt, C. 2008, ApJ, 674, 686

Xue, Y.-J., & Wu, X.-P. 2000, ApJ, 538, 65

Yoshino, T., et al. 2009, PASJ, 61, 805